

# Extremely Large Antenna Spacing Method for Enhanced Wideband Near-Field Sensing

Tommaso Bacchielli, *Graduate Student Member, IEEE*, Lorenzo Pucci, *Member, IEEE*,  
and Andrea Giorgetti, *Senior Member, IEEE*

**Abstract**—This paper proposes a monostatic wideband system for integrated sensing and communication (ISAC) at millimeter-wave frequencies, based on multiple-input multiple-output (MIMO) orthogonal frequency-division multiplexing (OFDM). The system operates in a hybrid near-/far-field regime. The transmitter (Tx) operates in the far field (FF) and uses low-complexity beam steering. The receiver (Rx), on the other hand, operates in a pervasive near field (NF), enabled by a very large effective array aperture. To enable a fully digital implementation, we introduce an extremely large antenna spacing (ELAS) design. This design attains the required aperture with only a few widely spaced antenna elements while avoiding grating lobes in the composite Tx–Rx response. We analytically characterize the NF range-angle response of this architecture and study the interplay between NF effects and waveform bandwidth. This leads to the definition of a super-resolution region, where NF propagation at the Rx dominates the achievable range resolution and surpasses the classical, bandwidth-limited resolution. As a case study, we consider an extended target modeled as a collection of scatterers and assess localization performance via maximum-likelihood estimation. Numerical results evaluated in terms of root mean square error (RMSE) and generalized optimal sub-pattern assignment (GOSPA) show that operating in NF conditions with the ELAS-based design yields significant gains compared to a conventional FF baseline at both the Tx and Rx.

**Index Terms**—Array signal processing, monostatic radar, near-field sensing, extended target, OFDM, super-resolution, integrated sensing and communication.

## I. INTRODUCTION

**T**HE rapid evolution of large-scale antenna technologies and high-frequency operation has fundamentally transformed the landscape of wireless sensing, especially in the context of integrated sensing and communication (ISAC) for next-generation wireless systems of sixth generation (6G) and beyond [1], [2]. As antenna apertures become extremely large, comparable to or even exceeding the operational wavelength by several orders of magnitude, the assumption of planar wavefronts, long adopted in classical far-field (FF) models, no longer holds [3]. Instead, electromagnetic propagation enters the near-field (NF) regime, where signals impinging on the

array exhibit spherical wavefronts and spatially varying amplitude and phase profiles across the antenna aperture [4], [5]. This transition to NF propagation offers new opportunities for high-precision sensing and localization [6], [7]. In particular, in this regime, the assumption that the passive target can be approximated as a point scatterer becomes insufficient, and the concept of extended targets (ETs) must be considered [8], [9]. In NF sensing, the curvature of the incident wavefront encodes valuable range-dependent spatial information that is otherwise lost under the FF approximation. This enables the joint estimation of range and angle parameters from a single array observation, effectively introducing an additional spatial degree of freedom [10]. As a consequence, NF systems can better distinguish multiple target scatterers located at similar angular positions but at different ranges [11]. This capability results in an enhanced range resolution compared to FF systems, where range resolution is solely determined by the bandwidth [12]. This property is especially beneficial for ET localization, where the target is modeled as a collection of multiple scattering contributions with distinct spatial positions and reflection coefficients.

Recent studies have analyzed the impact of NF on the sensing performance in both narrowband and wideband systems. In [13], the range resolution (or depth of focus (DF)) of an antenna under NF conditions is derived as the distance interval where the array gain remains within 3 dB of its peak. The work in [14] explores how array shape and size influence the NF beam behaviors in narrowband sensing systems and introduces a beam depth analysis for characterizing the NF beam patterns in the distance domain. Similarly, [15] investigates the ambiguity function of narrowband NF multiple-input multiple-output (MIMO) radar for different aperture geometries. In wideband NF systems, range resolution depends on the combined effect of bandwidth and NF. The latter can enhance resolution when bandwidth is limited, reducing the need for large bandwidths. However, the NF advantage on resolution diminishes with increasing target distance, unlike the robustness of wideband sensing, indicating that NF sensing alone cannot fully replace the capabilities of wideband sensing [16]. The study in [17] approximates the range ambiguity function of wideband NF systems, showing that when the resolution due to bandwidth is comparable to the NF beam focusing, the NF effect can improve the composite range profile by reducing sidelobes. Conversely, bandwidth expansion mitigates poor sidelobe levels in bandwidth-limited NF systems. Works such as [18], [19] evaluate the performance of wideband orthogonal frequency-division multiplexing (OFDM)-based ISAC systems

This work was supported by the European Union under the Italian National Recovery and Resilience Plan (NRRP) of NextGenerationEU, partnership on “Telecommunications of the Future” (PE00000001 - program “RESTART”).

T. Bacchielli and A. Giorgetti are with the Department of Electrical, Electronic, and Information Engineering “Guglielmo Marconi” (DEI), University of Bologna, and the National Laboratory of Wireless Communications (WiLab), CNIT, Italy (e-mail: {tommaso.bacchielli2, andrea.giorgetti}@unibo.it). L. Pucci is with the National Laboratory of Wireless Communications (WiLab), CNIT, Italy (e-mail: lorenzo.pucci@wilab.cnit.it). T. Bacchielli and L. Pucci are co-first authors.

that exploit both wavefront curvature and bandwidth to jointly estimate range and angle, enhancing spatial resolution. In [20] and [21], authors analyze wideband NF MIMO-OFDM systems, deriving Cramér-Rao lower bounds (CRLBs) for multi-target localization and demonstrating that array aperture and bandwidth, rather than the number of antennas and subcarriers, primarily determine sensing accuracy.

Despite these advantages, the deployment of extremely large aperture arrays (ELAAs) introduces significant practical and architectural challenges. Achieving a large physical aperture by simply increasing the number of antenna elements, as in extremely large-scale MIMO (XL-MIMO) architectures, leads to prohibitively high hardware complexity and energy consumption [22]. In particular, implementing such arrays with a fully digital architecture—where each antenna element is equipped with its own radio-frequency (RF) chain, including mixers, converters, and baseband processing units—is largely infeasible at large scale. In fact, this results in high power consumption and cost, and imposes stringent demands on synchronization, calibration, and real-time signal processing. These limitations have motivated the exploration of hybrid analog–digital architectures [23], [24], [25], [26], subarray structures [27], [28], and energy-efficient beamforming strategies to strike a balance between performance and implementation feasibility in large-scale NF sensing systems with ELAAs.

To the best of the authors’ knowledge, there remains a lack of research on practical, fully digital implementations of ELAAs that avoid the XL-MIMO paradigm and its associated, unfeasibly large number of antenna elements. Furthermore, a thorough analysis of the benefits of wideband NF sensing on range resolution and target position estimation accuracy, also supported by numerical simulations, has not yet been fully addressed. In particular, the literature does not clearly establish under which conditions the NF effect at the receiver (Rx) can enhance the range resolution of a wideband sensing system beyond what is achievable by bandwidth alone.

When equipped with ELAAs, sensing systems can effectively exploit NF propagation effects [29]. Such arrays are typically realized as uniform linear arrays (ULAs) with a very large physical aperture obtained by substantially increasing the number of antenna elements according to the XL-MIMO paradigm [30]. The large aperture not only improves angular resolution but also extends the Fraunhofer distance, which defines the theoretical boundary between near- and FF regions and grows quadratically with the aperture size [14]. As a result, NF characteristics persist over distances that are relevant for sensing operation, allowing the system to achieve high spatial (range and angular) resolution and to better distinguish closely spaced scattering points. This ultimately enhances the reconstruction of ETs that can be modeled as a set of distributed scatterers [23].

To address these unexplored aspects, we take as a starting point the transmit–receive array configuration with dissimilar element spacings introduced in [31] for narrowband MIMO radar, and generalize it to a fundamentally different operating regime—namely, a wideband MIMO ISAC system based on OFDM, operating at millimeter wave (mmWave) frequencies under hybrid NF and FF conditions.

This generalization departs from the narrowband, angle-only beampattern perspective of [31] by explicitly accounting for wideband signaling and near-field effects at the Rx, enabled through an extremely large effective aperture achieved via an extremely large antenna spacing (ELAS) design. The resulting framework allows us to investigate fundamental resolution limits and performance gains in hybrid near-/far-field ISAC systems. In particular, the main contributions are summarized as follows:

- 1) We design a monostatic wideband MIMO OFDM-based ISAC architecture that, by design, drives the Rx into a NF operating regime. Specifically, the transmitter (Tx) operates in the FF and can therefore rely on low-complexity beam steering rather than beam focusing, while the Rx operates under an all-pervasive NF condition induced by the extremely large effective aperture enabled by the ELAS design. This approach achieves NF sensing capabilities with only a limited number of antenna elements, in contrast to the very large arrays typically required in XL-MIMO systems.
- 2) We analytically characterize the impact of waveform bandwidth on the proposed hybrid near-/far-field architecture, going beyond the narrowband, angle-only beampattern analysis in [31]. By studying the NF range–angle response at the Rx, we identify a super-resolution region around the transceiver in which NF effects dominate the achievable range resolution and can significantly outperform classical bandwidth-limited resolution.
- 3) We validate the proposed ELAS-based design through numerical simulations, using a generalized likelihood ratio test (GLRT)-based framework for joint detection and target parameter estimation when modeling an ET as a collection of scattering points. The sensing performance is assessed in terms of root mean square error (RMSE) and generalized optimal sub-pattern assignment (GOSPA) metrics, demonstrating clear performance gains when operating under NF conditions at the Rx compared to a conventional baseline assuming FF propagation at both the Tx and the Rx.

In this paper, bold uppercase and lowercase letters denote matrices and vectors, respectively.  $\mathbf{I}_n$  is the  $n \times n$  identity matrix, and  $\text{diag}(\cdot)$  represents the diagonal matrix. The operators  $(\cdot)^*$ ,  $(\cdot)^T$ , and  $(\cdot)^H$  denote conjugation, transpose, and conjugate transpose, respectively. We use  $\text{card}(\cdot)$ ,  $|\cdot|$ ,  $\|\cdot\|$ , and  $\otimes$  for cardinality, modulus, Euclidean norm, and Kronecker product, respectively, and  $\mathbb{E}[\cdot]$  for expectation. A zero-mean circularly symmetric complex Gaussian random vector with covariance matrix  $\Sigma$  is denoted as  $\mathbf{x} \sim \mathcal{CN}(\mathbf{0}, \Sigma)$ , and  $x \sim \mathcal{B}(q, n)$  represents a Binomial random variable with number of trials  $n$  and success probability  $q$ .

The remainder of the paper is organized as follows. Section II introduces the system model. Section III presents the proposed ELAS method, while Section IV analyzes the impact of near-field propagation and bandwidth on range resolution. Section V describes the GLRT-based detection and parameter estimation framework. Numerical results are reported in Section VI, and Section VII concludes the paper.

## II. SYSTEM MODEL

In this work, we consider a monostatic MIMO OFDM-based ISAC transceiver with full-duplex operation, as depicted in Fig. 1.<sup>1</sup>

To perform sensing tasks, OFDM frames consisting of  $M$  OFDM symbols with  $K$  contiguous active subcarriers are transmitted. The  $k$ -th subcarrier has frequency  $f_k = f_c + (k - K/2)\Delta f$  with  $k = 0, \dots, K - 1$ , where  $f_c$  is the carrier frequency and  $\Delta f$  is the subcarrier spacing. The total frame duration is  $MT_s$ , where  $T_s \triangleq \frac{1}{\Delta f} + T_{cp}$  is the OFDM symbol duration including the cyclic prefix (CP), and the total bandwidth is  $B = K\Delta f$ . Throughout this work, we assume that the system operates with  $f_c \gg B$ , so that the narrowband array response assumption holds for each subcarrier [33].

Both the Tx and Rx are equipped with a ULA aligned along the  $y$ -axis, composed of  $N_t$  and  $N_r$  antenna elements with inter-element spacings  $d_t$  and  $d_r$ , respectively, with  $d_r \gg d_t$  [31]. The Tx array is placed at  $\mathbf{p}^{tx} = [0, 0]^T$ , and has an aperture  $D_t = (N_t - 1)d_t$ . We consider relatively small transmit apertures such that the corresponding Fraunhofer distance  $D_F^{tx} = 2D_t^2/\lambda$  is much smaller than the distances of interest in the monitored area. Hence, the Tx can be modeled as operating under FF propagation conditions.

The  $n$ -th Rx antenna element is located at

$$\mathbf{p}_n^{rx} = [x_n^{rx}, y_n^{rx}]^T = [0, \tilde{n}d_r]^T, \quad n = 1, \dots, N_r \quad (1)$$

with  $\tilde{n} = \frac{2n - N_r - 1}{2}$ , leading to the Rx aperture

$$D_r = (N_r - 1)d_r. \quad (2)$$

We assume that the sensing system monitors an area whose maximum Euclidean distance from the transceiver, denoted by  $r_{\max}$ , satisfies

$$r_{\max} \ll D_F^{rx} = \frac{2D_r^2}{\lambda} \quad (3)$$

where  $D_F^{rx}$  denotes the Fraunhofer distance with respect to the Rx,  $\lambda = c/f_c$  is the wavelength and  $c$  is the speed of light. Under this condition, the propagation with respect to the Rx is such that NF effects can be exploited for sensing.

The specific choice of the inter-element spacings  $d_t$  and  $d_r$  is based on an antenna spacing design that enables a huge effective aperture at the Rx while using a limited number of antenna elements. This design, referred to as the ELAS method, is inspired by the approach proposed in [31] and is detailed in Section III.

### A. Input-Output Relationship

The complex baseband OFDM signal transmitted by the Tx antenna array is expressed in vector form as<sup>2</sup>

$$\mathbf{s}(t) = \sqrt{\frac{P_t G_t}{K}} \mathbf{w}_t \sum_{m=0}^{M-1} \left( \sum_{k=0}^{K-1} x[k, m] e^{j2\pi k \Delta f t} \right) g_{tx}(t - mT_s) \quad (4)$$

<sup>1</sup>A monostatic radar setup requires a full-duplex architecture employing analog/digital self-interference (SI) cancellation methods (see, e.g., [32]). In this work, we assume that the SI is effectively suppressed and therefore negligible compared to Gaussian noise at the sensing Rx.

<sup>2</sup>To simplify the notation, the CP is omitted in (4), although it is implicitly included to guarantee robustness against inter-symbol interference (ISI).

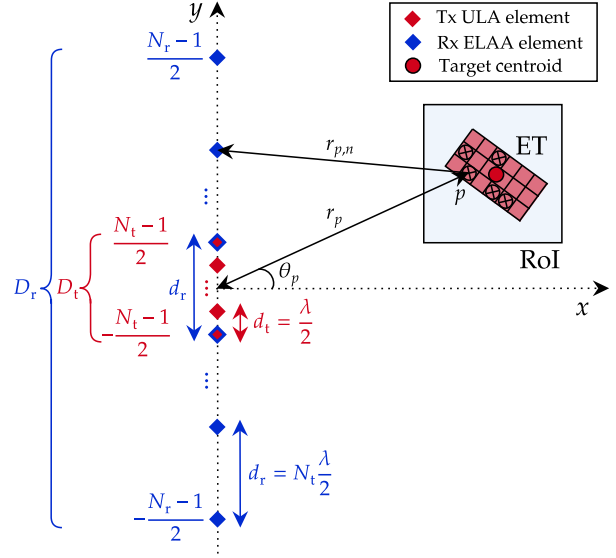


Figure 1: Monostatic MIMO ISAC setup with hybrid near-/far-field operation. The system is composed of a Tx ULA with half-wavelength spacing and a sparsely spaced Rx ELAA implementing the ELAS design to observe an ET located in the area of interest.

where  $P_t$  is the total transmit power,  $G_t$  is the single antenna element gain at the Tx,  $\mathbf{w}_t \in \mathbb{C}^{N_t \times 1}$  is the beamforming weight vector designed based on the application (more details will be provided later),  $x[k, m]$  denotes a generic complex modulation symbol transmitted at time instant  $m$  on subcarrier  $k$  and normalized so that  $\mathbb{E}\{|x[k, m]|^2\} = 1$ , while  $g_{tx}(t)$  represents the modulating pulse.

At the Rx, after the fast Fourier transform (FFT) block for OFDM demodulation, a received time-frequency grid of complex elements  $y[k, m]$  is obtained at each antenna element. By considering negligible inter-carrier interference (ICI) and ISI, the vector  $\mathbf{y}[k, m] \in \mathbb{C}^{N_r \times 1}$  of received complex modulation symbols at subcarrier  $k$  for  $m$ -th OFDM symbol is given by

$$\mathbf{y}[k, m] = \sqrt{\frac{P_t G_t G_r}{K}} \mathbf{H}[k, m] \mathbf{w}_t x[k, m] + \boldsymbol{\nu}[k, m] \quad (5)$$

where  $G_r$  is the single antenna element gain of the Rx,  $\mathbf{H}_{t,r}[k, m] \in \mathbb{C}^{N_r \times N_t}$  is the MIMO channel matrix in the frequency domain for the subcarrier  $k$  at time  $m$  which is defined in Section II-B. Moreover,  $\boldsymbol{\nu}[k, m] \sim \mathcal{CN}(\mathbf{0}, \sigma_\nu^2 \mathbf{I}_{N_r})$  represents the additive white Gaussian noise (AWGN), with noise variance  $\sigma_\nu^2 = N_0 \Delta f$ , where  $N_0 = k_B T_0 n_F$  is the noise power spectral density,  $k_B$  is the Boltzmann constant,  $T_0 = 290$  K, and  $n_F$  is the Rx noise figure.

### B. Channel and Target Model

Without loss of generality, this work considers a single ET scenario, where the ET is modeled as a set of grid elements  $\mathcal{E}$  within a designated rectangular region  $\mathcal{A} \subset \mathbb{R}^2$  with a fixed size of length  $L$  and width  $W$  and an area of  $|\mathcal{A}| = LW$ , as proposed in [23] (see Fig. 1). The decision to model the target as an extended object is based on the assumption that the Rx is operating in NF conditions. Therefore, it is reasonable to

assume that the target can be seen as a set of scatterers from the Rx perspective.

At each time measurement, the ET is composed of a random number  $P < |\mathcal{E}|$  of micro-scatterers. Given that each grid element inside  $\mathcal{A}$  can be active, i.e., the scatterer is localized inside that element, with probability  $q$ , the number of active points, or target scatterers, follows a binomial distribution, i.e.,  $P \sim \mathcal{B}(q, |\mathcal{E}|)$ . With an appropriate choice of the grid size, the varying number of scatterers in the target area can effectively model the fluctuations and variance of an object's radar reflectivity caused by factors such as, e.g., target aspect angle and material. Hereinafter, we refer to the scatterers of the ET as micro-scatterers to emphasize that they represent reflective points of a larger object.

Considering line of sight (LoS) propagation conditions and accounting for all the visible micro-scatterers from the ET, the  $N_r \times N_t$  hybrid near-/far-field MIMO channel matrix in (5) for subcarrier  $k$  at time  $m$  can be written as

$$\mathbf{H}[k, m] = \sum_{p=1}^P \epsilon_p e^{j2\pi(mT_s f_{D,p} - k\Delta f \tau_p)} \mathbf{b}(\theta_p, r_p) \mathbf{a}^H(\theta_p) \quad (6)$$

where  $r_p$  is the reference Euclidean distance between the center of the transceiver and the  $p$ -th micro-scatterer,  $\tau_p = 2r_p/c$  is the corresponding reference round-trip delay related to the micro-scatterer  $p$  and  $f_{D,p} = 2v_p f_c/c$  is the reference Doppler shift associated with the  $p$ -th micro-scatterer, with  $v_p$  its relative radial velocity. Moreover,  $\epsilon_p = \sqrt{\frac{\sigma_p c^2}{(4\pi)^3 f_c^2 r_p^4}} e^{-j2\pi f_c \tau_p}$  is the reference complex channel factor, and  $\sigma_p$  is the radar cross-section (RCS) associated with micro-scatterer  $p$ . The FF transmit and NF receive array responses, denoted by  $\mathbf{a}(\theta_p) \in \mathbb{C}^{N_t \times 1}$  and  $\mathbf{b}(\theta_p, r_p) \in \mathbb{C}^{N_r \times 1}$ , respectively, are defined as [23]

$$\mathbf{a}(\theta_p) = \left[ e^{-j\frac{N_t-1}{2}\pi \sin(\theta_p)}, \dots, e^{j\frac{N_t-1}{2}\pi \sin(\theta_p)} \right]^T \quad (7)$$

$$\mathbf{b}(\theta_p, r_p) = \left[ \frac{r_p}{r_{p,1}} e^{-j\frac{2\pi}{\lambda}(r_{p,1}-r_p)}, \dots, \frac{r_p}{r_{p,n}} e^{-j\frac{2\pi}{\lambda}(r_{p,n}-r_p)}, \dots, \frac{r_p}{r_{p,N_r}} e^{-j\frac{2\pi}{\lambda}(r_{p,N_r}-r_p)} \right]^T \quad (8)$$

where  $r_p$  and  $\theta_p$  are the reference distance and reference angle of departure (AoD)/angle of arrival (AoA), respectively, between the Tx/Rx and the scatterer  $p$ , calculated with respect to the geometric center of the array at  $[0, 0]^T$ .<sup>3</sup> In (8),  $r_{p,n}$  denotes the Euclidean distance between the scatterer  $p$  and the  $n$ -th receive antenna. If the scatterer  $p$  is located at  $\mathbf{p}_p = [x_p, y_p]^T = [r_p \cos(\theta_p), r_p \sin(\theta_p)]^T$ , this distance can be expressed as [1]

$$r_{p,n} = \|\mathbf{p}_p - \mathbf{p}_n^{\text{rx}}\| = r_p \sqrt{1 + \frac{(\tilde{n}d_r)^2}{r_p^2} - \frac{2\tilde{n}d_r \sin(\theta_p)}{r_p}}. \quad (9)$$

where  $\tilde{n}$  is provided in (1).

<sup>3</sup>Note that, in practice, the Tx and Rx antennas may be separated by a small distance. Here, for simplicity, we assume that their phase centers coincide at the origin. This approximation is accurate when the Tx–Rx separation is negligible compared to the target ranges, and any residual offset can be accounted for through calibration.

A second-order Taylor expansion can accurately approximate such a distance, also known as the Fresnel approximation [34], [35], [36], i.e.,

$$r_{p,n} \approx r_p - \tilde{n}d_r \sin(\theta_p) + \frac{(\tilde{n}d_r \cos(\theta_p))^2}{2r_p}. \quad (10)$$

Note that, under FF conditions,  $r_p \simeq r_{p,n}$  and  $r_p \gg \tilde{n}d_r$  for all  $n$ . In this regime, the Rx array response loses its dependence on the distance  $r_p$  and reduces to the well-known FF array response vector as per (7).

### III. PROPOSED EXTREMELY LARGE ANTENNA SPACING (ELAS) METHOD FOR NEAR-FIELD SENSING

As previously mentioned, in this work, we deliberately consider a Tx array with a limited aperture, so that its Fraunhofer distance  $D_F^{\text{tx}}$  is much smaller than the target ranges of interest. Under this design choice, the Tx can be modeled as operating in the FF for all points in the monitored area, thus eliminating the need for a beam focusing scheme at the Tx, which can be challenging and computationally demanding for some applications due to the joint search over range and angle [23]. Instead, a straightforward beam steering approach is adopted to illuminate the monitored area. Conversely, the considered Rx is an ELAA with an aperture large enough for the entire monitored area to lie in the effective NF of the antenna.<sup>4</sup> This configuration enables enhanced spatial (range and angle) resolution, thereby improving target localization accuracy.

A common way to realize such an ELAA is to employ a ULA with a very large number of antennas and an inter-element spacing of  $\lambda/2$ . This avoids undesired grating lobes (i.e., ambiguities) in the angle domain. However, such a design may be challenging from a hardware implementation viewpoint and highly expensive. In fact, when the number of antennas becomes very large, current fully digital and hybrid implementations do not scale well in terms of complexity, power consumption, and latency.

To explore a lower-complexity solution, we adopt an antenna spacing scheme where the Tx and Rx arrays are designed to yield a composite response equivalent to that of an  $N_t N_r$ -element array with  $\lambda/2$  spacing, as in [31]. In particular, the Tx antennas are spaced by  $d_t = \lambda/2$ , whereas at the Rx the inter-element spacing is chosen as  $d_r = N_t \lambda/2$ , i.e., much larger than  $\lambda/2$ . Such a spacing at the Rx would, in principle, generate grating lobes (ambiguities) in the angle response. However, thanks to the combination of the Tx and Rx array responses, the grating lobes are effectively suppressed in the composite Tx–Rx array response. While the analysis in [31] is limited to the composite beam pattern in a narrowband, FF regime, in the following, we explicitly characterize the individual transmit and receive angle responses, as well as their

<sup>4</sup>It is worth noting that the effective NF region, from a sensing perspective, is typically much smaller than the region implied by the Fraunhofer distance, approximately within one seventh of that distance [15]. In fact, the classical Fraunhofer distance is defined based on the phase error of the far-field approximation with respect to the accurate NF model, which may not effectively reflect sensing performance in terms of resolution and localization accuracy [1], [3].

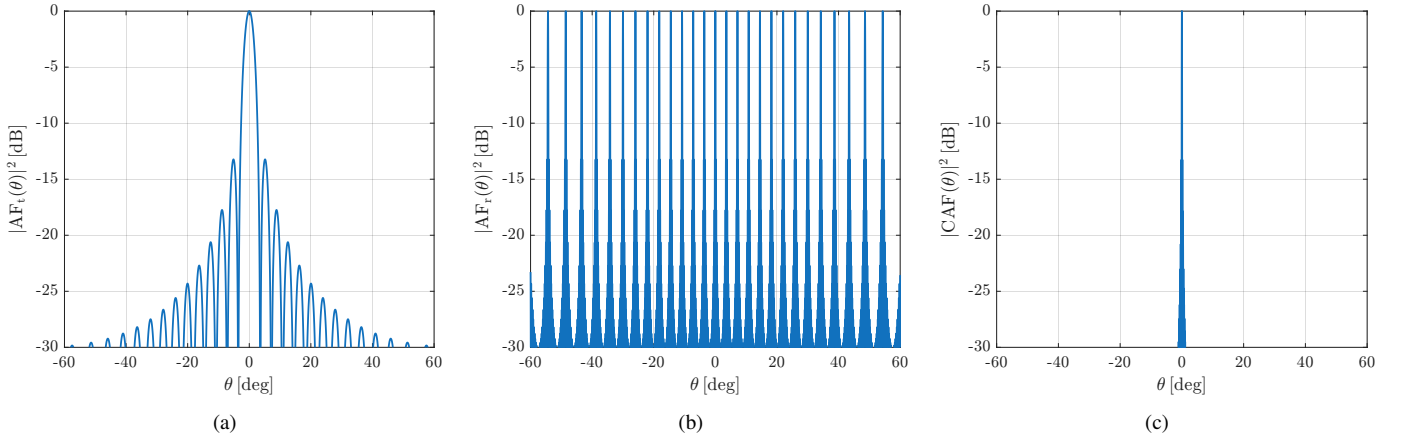


Figure 2: Normalized Tx FF array factor (a), Rx NF array factor (b), and composite array factor (c) evaluated in the angular domain under the angular sampling method assumption, by considering the proposed monostatic radar configuration with the following system parameters:  $f_c = 60$  GHz,  $d_t = \lambda/2$ ,  $d_r = N_t \lambda/2$  and  $N_t = N_r = 32$ .

composite response. We show that this architecture realizes a hybrid near-/far-field system, with the Tx operating in the FF (i.e., with reduced complexity) and the Rx in the NF (i.e., with enhanced target localization accuracy), and analyze the impact of the signal bandwidth on localization performance.

#### A. Far-Field Tx Array Factor

As previously described, the Tx employs a ULA with  $N_t$  elements and spacing  $d_t = \lambda/2$ , operating in the FF over the monitored area. With reference to (7), we adopt a beam steering approach with beamforming weights  $\mathbf{w}_t = \mathbf{a}(\bar{\theta})$ , where  $\bar{\theta}$  is the desired pointing direction, where, e.g., a potential target can be present.

The normalized Tx array factor is given by

$$\begin{aligned} \text{AF}_t(\theta) &= \frac{1}{N_t} \mathbf{a}^H(\theta) \mathbf{w}_t = \frac{1}{N_t} \mathbf{a}^H(\theta) \mathbf{a}(\bar{\theta}) \\ &= \frac{1}{N_t} \sum_{n=-\frac{N_t-1}{2}}^{\frac{N_t-1}{2}} e^{j\pi n (\sin(\bar{\theta}) - \sin(\theta))} \\ &= \frac{1}{N_t} \frac{\sin(N_t \pi/2 (\sin(\theta) - \sin(\bar{\theta})))}{\sin(\pi/2 (\sin(\theta) - \sin(\bar{\theta})))}. \end{aligned} \quad (11)$$

Note that, the expression of the normalized Tx array factor  $\text{AF}_t$  in (11) has the form of the *Dirichlet kernel*  $D_{\frac{N_t-1}{2}}((\sin(\theta) - \sin(\bar{\theta}))/2)$ . From the properties of this periodic function, its amplitude exhibits a main lobe in correspondence with the illuminated direction  $\theta = \bar{\theta}$  and many secondary lobes of decreasing amplitude with periodic notches at

$$\theta_{\text{notch},i}^{\text{tx}} = \arcsin((2i/N_t) + \sin(\bar{\theta})) \quad (12)$$

for  $i \in \mathbb{Z} \setminus \{0\}$ , as illustrated in Fig. 2a. The angular resolution of the transmit array is determined by the main-lobe width of its (normalized) power beampattern  $|\text{AF}_t(\theta)|^2$ , and is conventionally quantified by the 3 dB beamwidth, i.e.,  $\Delta\theta_{3\text{dB}}^{\text{tx}} \approx 0.89\lambda/D_t \approx 2/N_t$  [37].

#### B. Near-Field Rx Array Factor

The Rx is designed to operate as an ELAA, providing effective NF conditions over the entire monitored area. As already mentioned, this is achieved by adopting the ELAS design [31], in which the Rx ULA has  $N_r$  elements with inter-element spacing  $d_r = N_t \frac{\lambda}{2}$ , thus realizing a very large aperture by increasing the spacing rather than the number of antennas. This choice contrasts with the conventional  $\lambda/2$  spacing typically used to avoid grating lobes and ambiguity issues in AoA estimation.

To derive the Rx array factor under the above assumptions, we consider a beam focusing approach in which the receive weight vector  $\mathbf{w}_r \in \mathbb{C}^{N_r \times 1}$  is given by  $\mathbf{w}_r = \mathbf{b}(\bar{\theta}, \bar{r})$  with  $\mathbf{b}(\theta, r)$  reported in (8). Here,  $(\bar{\theta}, \bar{r})$  represents the polar coordinates of a generic focus point with respect to the center of the Rx antenna array. The normalized NF array factor at the Rx can be expressed as

$$\begin{aligned} \text{AF}_r(\theta, r) &= \frac{1}{N_r} \mathbf{w}_r^H \mathbf{b}(\theta, r) = \frac{1}{N_r} \mathbf{b}^H(\bar{\theta}, \bar{r}) \mathbf{b}(\theta, r) \\ &\approx \frac{1}{N_r} \sum_{n=-\frac{N_r-1}{2}}^{\frac{N_r-1}{2}} e^{-j\pi N_t^2 \frac{\lambda}{4} n^2 \left( \frac{\cos^2(\theta)}{r} - \frac{\cos^2(\bar{\theta})}{\bar{r}} \right)} \\ &\quad \times e^{j\pi N_t n (\sin(\theta) - \sin(\bar{\theta}))}. \end{aligned} \quad (13)$$

Note that the NF array factor at the Rx in (13) cannot, in general, be expressed with a simple closed form due to its joint dependence on the AoA  $\theta$  and the range  $r$ . To gain further insight, we follow the approach in [4], which introduces two sampling methods, the *angular sampling method* and the *distance sampling method*, that decouple the array factor into angle-only and range-only components under suitable assumptions. In the following, we employ these methods to study the Rx array factor separately in the angular and range domains and derive closed-form expressions in each domain.

1) *Near-field Rx array factor in the angular domain*: The derivation of the Rx array factor in (13) in the angular domain follows the angular sampling method in [4]. The key idea is to

evaluate  $AF_r$  at points in polar coordinates  $(\theta, r)$  that satisfy

$$\frac{\cos^2(\theta)}{r} = \frac{\cos^2(\bar{\theta})}{\bar{r}} = \frac{1}{R} \quad (14)$$

where  $R > 0$  is a given constant. Equivalently, we restrict the analysis to locations lying on the curve  $r = R \cos^2(\theta)$ , which we refer to as the *distance ring*  $R$ , in analogy with [4].

Under this condition, the quadratic phase term in (13), which originally depends jointly on angle and range, vanishes, and the normalized array factor becomes only a function of the AoA, as follows

$$\begin{aligned} AF_r(\theta) &\approx \frac{1}{N_r} \sum_{n=-\frac{N_r-1}{2}}^{\frac{N_r-1}{2}} e^{j\pi N_t n (\sin(\theta) - \sin(\bar{\theta}))} \\ &= \frac{1}{N_r} \frac{\sin(N_r N_t \pi / 2 (\sin(\theta) - \sin(\bar{\theta})))}{\sin(N_t \pi / 2 (\sin(\theta) - \sin(\bar{\theta})))}. \end{aligned} \quad (15)$$

It is worth noting that, in those regions of space where the range dependence can be removed, the NF array factor at the Rx observed in the angular domain exhibits the same Dirichlet-kernel structure as the FF Tx array factor in (11), but with an effectively larger aperture. However, differently from the Tx, the Rx array response shows periodic grating lobes at

$$\theta_{gl,i}^{rx} = \arcsin\left(\frac{2i}{N_t} + \sin(\bar{\theta})\right) \quad (16)$$

for  $i \in \mathbb{Z} \setminus \{0\}$ , as shown in Fig. 2b. This is caused by the Rx inter-element spacing  $d_r = N_t \lambda / 2$ , which is larger by a factor of  $N_t$  than the conventional half-wavelength spacing. In Section III-C, we show that these angle ambiguities in the Rx array factor are eliminated in the composite Tx–Rx array factor, which is equivalent to that of a virtual array with  $N_t N_r$  elements spaced by  $\lambda / 2$ . Consequently, under the proposed ELAS design, the 3dB beamwidth is effectively that of a half-wavelength array with  $N_t N_r$  elements, i.e.,  $\Delta\theta_{3dB}^{rx} \approx 0.89\lambda / D_r \approx 2 / (N_t N_r)$  [37].

2) *Near-field Rx array factor in the range domain*: Similarly, the NF Rx array factor in the range domain can be evaluated according to the distance sampling method proposed in [4]. This method eliminates the dependence of the NF array factor on the AoA, by fixing a generic observation direction, i.e.,  $\theta = \bar{\theta}$ . It follows that

$$AF_r(r) = \frac{1}{N_r} \sum_{n=-\frac{N_r-1}{2}}^{\frac{N_r-1}{2}} e^{-j\pi N_t^2 \frac{\lambda}{4} \cos^2(\bar{\theta}) n^2 \left(\frac{1}{r} - \frac{1}{\bar{r}}\right)}. \quad (17)$$

In contrast to the angular sampling case, the quadratic phase term in (17) makes it difficult to obtain a simple closed-form expression. However, [4] shows that  $AF_r(r)$  can be very accurately approximated in terms of Fresnel functions as

$$AF_r(r) \approx F(\Xi) = \frac{C(\Xi) + jS(\Xi)}{\Xi} \quad (18)$$

where  $\Xi = N_r N_t \cos(\bar{\theta}) \sqrt{\frac{\lambda}{8} \left| \frac{1}{r} - \frac{1}{\bar{r}} \right|}$ , while  $C(\Xi) = \int_0^\Xi \cos\left(\frac{\pi}{2} t^2\right) dt$  and  $S(\Xi) = \int_0^\Xi \sin\left(\frac{\pi}{2} t^2\right) dt$  are the Fresnel functions [38].

Note that the profile of  $AF_r(r)$  depends on the focusing range  $\bar{r}$  through the parameter  $\Xi$ , as illustrated in Fig. 3.

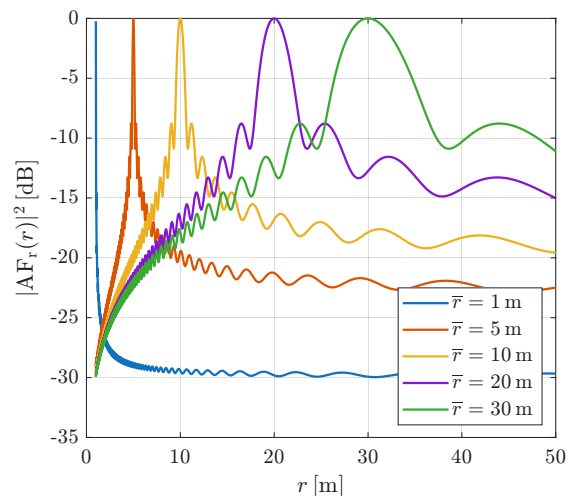


Figure 3: Rx NF array factor in the range domain under the distance sampling method assumption [4], obtained focusing at multiple distances  $\bar{r}$  from the transceiver at  $\bar{\theta} = 0^\circ$  with  $f_c = 60$  GHz,  $d_t = \lambda / 2$ ,  $d_r = N_t \lambda / 2$  and  $N_t = N_r = 32$ .

In particular, the range resolution determined solely by the NF conditions at the ELAA Rx varies with  $\bar{r}$ , becoming significantly finer for targets located closer to the array.

### C. Composite Array Factor

Referring to the channel model in (6), let us consider a single scatterer, i.e.,  $P = 1$ , with AoD/AoA  $\bar{\theta}$  and range  $\bar{r}$ . The corresponding MIMO channel contribution is proportional to the outer product of the transmit and receive array responses, i.e.,  $\mathbf{H}(\bar{\theta}, \bar{r}) \propto \mathbf{b}(\bar{\theta}, \bar{r}) \mathbf{a}^H(\bar{\theta})$ . When transmit beam steering with  $\mathbf{w}_t = \mathbf{a}(\bar{\theta})$  and receive beam focusing with  $\mathbf{w}_r = \mathbf{b}(\bar{\theta}, \bar{r})$  are applied, the effective scalar response toward a generic point  $(\theta, r)$  is given by

$$\mathbf{w}_r^H \mathbf{H}(\theta, r) \mathbf{w}_t \propto (\mathbf{a}^H(\theta) \mathbf{w}_t) (\mathbf{w}_r^H \mathbf{b}(\theta, r)).$$

After normalization, the two factors in parentheses correspond exactly to the transmit and receive array factors defined in (11) and (13). Under the assumptions of the angular sampling method, this motivates defining the normalized composite array factor in the angular domain as

$$\begin{aligned} CAF(\theta) &= AF_t(\theta) AF_r(\theta) \\ &= \frac{1}{N_t N_r} \frac{\sin(N_r N_t \pi / 2 (\sin(\theta) - \sin(\bar{\theta})))}{\sin(\pi / 2 (\sin(\theta) - \sin(\bar{\theta})))}. \end{aligned} \quad (19)$$

By comparing (19) with the Tx array factor in (11), it is clear that the composite array factor has the same form as the beampattern of a virtual ULA with  $N_t N_r$  elements spaced by  $\lambda / 2$ , thus providing a much larger effective aperture and finer angular resolution, determined by the Rx array as  $\Delta\theta_{3dB} \equiv \Delta\theta_{3dB}^{rx} \approx 2 / (N_t N_r)$  (see Section III-B).

As illustrated in Fig. 2c, this behavior is due to the fact that the proposed Rx spacing  $d_r = N_t \lambda / 2$  aligns the Rx grating lobes with the Tx notches. Indeed, from (12) and (16) it follows that  $\theta_{gl,i}^{rx} \equiv \theta_{notch,i}^{tx}$  for  $i \in \mathbb{Z} \setminus \{0\}$ .

In the range domain, the composite array factor coincides with the Rx array factor  $AF_r(r)$ . In fact, for the FF Tx model

adopted in this work, the transmit array factor depends only on the angle and not on the range. When we fix the observation angle to the steering direction, i.e.,  $\theta = \bar{\theta}$ , the normalized Tx array factor evaluates to  $\text{AF}_t(\bar{\theta}) = 1$ , so that

$$\text{CAF}(r) = \text{AF}_t(\bar{\theta}) \text{AF}_r(r) = \text{AF}_r(r). \quad (20)$$

Using the distance sampling method previously introduced, this can be further written as per (18).

#### IV. JOINT BEAM FOCUSING AND BANDWIDTH EFFECTS FOR ENHANCED RANGE RESOLUTION

In the previous section, the composite array response of the proposed MIMO architecture was characterized by focusing on its angular and range behavior under a narrowband assumption. We now investigate how the range response related to the sole array interacts with the waveform bandwidth in a wideband OFDM system, and how their joint effect determines the achievable range resolution. In particular, in this section, we show that NF propagation at the Rx can create a super-resolution region in which the array-induced range resolution surpasses the classical bandwidth-limited one, while the bandwidth still plays a key role in controlling sidelobe levels in the overall range profile. Effective NF conditions can significantly enhance the sensing range resolution, even in wideband systems. In an NF sensing system, the range resolution is determined by the joint effect of the waveform bandwidth and the NF beam focusing operation enabled by ELAAs. To highlight this interaction, we first recall the classical bandwidth-limited range profile.

For the considered monostatic configuration, the bandwidth  $B$  impacts the range resolution according to the Rayleigh criterion as  $\Delta r_B = \frac{c}{2B}$ , where  $\Delta r_B$  is defined as the distance between the main-lobe peak and the first null of the range profile. For the considered OFDM system, we define the frequency steering vector for a target at range  $r$  as

$$\mathbf{g}(r) = [e^{-j2\pi f_0 \frac{2r}{c}}, \dots, e^{-j2\pi f_k \frac{2r}{c}}, \dots, e^{-j2\pi f_{K-1} \frac{2r}{c}}]^T. \quad (21)$$

When focusing at range  $\bar{r}$ , the corresponding weighting vector is  $\mathbf{w}_B = \mathbf{g}(\bar{r})$ , and the normalized bandwidth-only range profile, by removing the common carrier term from  $f_k$ , can be expressed as

$$\begin{aligned} \text{RP}_B(r) &= \frac{1}{K} \mathbf{w}_B^H \mathbf{g}(r) = \frac{1}{K} \mathbf{g}^H(\bar{r}) \mathbf{g}(r) \\ &= \frac{1}{K} \sum_{k=-\frac{K-1}{2}}^{\frac{K-1}{2}} e^{-j2\pi k \Delta f \frac{2(r-\bar{r})}{c}} \\ &= \frac{1}{K} \frac{\sin(K \Delta f 2\pi(r-\bar{r})/c)}{\sin(\Delta f 2\pi(r-\bar{r})/c)}. \end{aligned} \quad (22)$$

On the other hand, the NF beam focusing effect also contributes to the range resolution, often described in terms of the DF of the array [1]. In this work, we follow the common convention in the NF literature and characterize the DF by the width of the range interval over which the power of the NF array factor remains above a fraction of its peak value.

Specifically, under the distance sampling method, we define the DF through the condition

$$|\text{CAF}(\bar{r} + \Delta r)|^2 = |\text{AF}_r(\bar{r} + \Delta r)|^2 \geq \frac{1}{2}. \quad (23)$$

Using the Fresnel-function approximation in (18), the condition in (23) can be rewritten as

$$|F(\Xi)|^2 \geq \frac{1}{2} \quad (24)$$

which is equivalent to  $|\Xi| \leq \Xi_{3\text{dB}}$  [4], where  $\Xi_{3\text{dB}}$  is such that  $|F(\Xi_{3\text{dB}})|^2 = 0.5$  and is approximately equal to  $\Xi_{3\text{dB}} \approx 1.318$ . This leads to the constraint  $|\frac{1}{r} - \frac{1}{\bar{r}}| \leq \frac{1}{r_{\text{DF},r}}$ , where,  $r_{\text{DF},r}$  is commonly referred to as the effective NF (or maximum focusing) distance with respect to the Rx. For the proposed setup with  $d_r = N_t \lambda / 2$ , the latter is given by

$$r_{\text{DF},r} \approx \frac{N_r^2 d_r^2 \cos^2(\bar{\theta})}{2\lambda \Xi_{3\text{dB}}^2} = \frac{N_r^2 N_t^2 \lambda \cos^2(\bar{\theta})}{8 \Xi_{3\text{dB}}^2}. \quad (25)$$

By recalling (3), for the proposed Rx ELAA, the Fraunhofer distance is  $D_F^{\text{rx}} = \frac{N_t(N_r-1)^2 \lambda}{2}$ . For  $\bar{\theta}$  close to broadside (so that  $\cos^2(\bar{\theta}) \approx 1$ ) and large  $N_r$ , and using the value of  $\Xi_{3\text{dB}}$  given above, (25) can be rewritten as<sup>5</sup>

$$r_{\text{DF},r} \approx \frac{N_r^2}{4 \Xi_{3\text{dB}}^2 (N_r - 1)^2} D_F^{\text{rx}} \approx \frac{D_F^{\text{rx}}}{6.952}. \quad (26)$$

Solving the inequality above for  $r = \bar{r} + \Delta r$  yields [1], [3]

$$\Delta r \in \left[ -\frac{\bar{r}^2}{r_{\text{DF},r} + \bar{r}}, \frac{\bar{r}^2}{\max(r_{\text{DF},r} - \bar{r}, 0)} \right]. \quad (27)$$

The interval above defines the range span around  $\bar{r}$  where the power of the NF array factor remains above 0.5 of its peak, and its width is therefore interpreted as the DF of the array. Thus, beam focusing is effectively achievable only within a limited fraction of the classical Fraunhofer distance, and the impact of the NF on the range resolution is confined to this focusing region. In particular, the DF of the Rx when performing beam focusing in direction  $\bar{\theta}$  and at a distance  $\bar{r}$  is given by [1]

$$\text{DF}_r(\bar{r}) = \begin{cases} \frac{2\bar{r}^2 r_{\text{DF},r}}{r_{\text{DF},r}^2 - \bar{r}^2} & \bar{r} < r_{\text{DF},r} \\ \infty & \bar{r} \geq r_{\text{DF},r}. \end{cases} \quad (28)$$

It is worth noting from (28) that the DF depends on the range  $\bar{r}$  of the focused location. In particular, it tends to infinity if the focus distance  $\bar{r}$  is larger than the threshold  $r_{\text{DF},r}$ , i.e., the focused location is outside the effective NF region. This implies that beam focusing degenerates to beam steering, since the orthogonality in the distance domain is almost lost. On the other hand, the range resolution greatly enhances when targets approach the Rx ELAA, as shown in Fig. 3.

From (18), (20), and (22), the overall range profile, taking into account both the bandwidth and the beam focusing

<sup>5</sup>The values of  $\Xi_{3\text{dB}}$  and, consequently,  $r_{\text{DF},r}$  are derived according to [15] for a single-input multiple-output (SIMO) ULA, i.e., considering only the receive array and ignoring the transmit contribution. This is consistent with the present architecture with dissimilar element spacings, where the Tx is assumed to operate in the FF and thus does not affect the distance-domain focusing behavior. The reader is referred to [15] for a more comprehensive treatment of  $\Xi_{3\text{dB}}$  and  $r_{\text{DF},r}$  across different array architectures.

effects, can be evaluated under the distance sampling method assumptions as

$$\begin{aligned} \text{RP}(r) &= \text{RP}_B(r) \text{CAF}(r) \\ &\approx \frac{1}{K} \frac{\sin(K\Delta f 2\pi(r - \bar{r})/c)}{\sin(\Delta f 2\pi(r - \bar{r})/c)} F(\Xi(r)). \end{aligned} \quad (29)$$

As shown in Fig. 4, when focusing at distances  $\bar{r}$  relatively close to the Rx, the overall range resolution of the system is determined by  $\text{DF}_r(\bar{r})$ , which is smaller than the bandwidth-limited Rayleigh range resolution  $\Delta r_B$ , and is therefore significantly enhanced compared to conventional radars. In contrast, as the focusing distance  $\bar{r}$  increases and  $\text{DF}_r(\bar{r})$  becomes larger than  $\Delta r_B$ , the overall range resolution is dominated by the bandwidth and coincides with  $\Delta r_B$ . This defines a *super-resolution region* around the Rx, where the range resolution is improved beyond the classical bandwidth-limited resolution due to the dominant contribution of the NF. This super-resolution region is contained within the effective NF area and is bounded by the distance  $r_{\text{sr}}$  from the Rx, defined as (in a monostatic setup)

$$r_{\text{sr}} \triangleq \sqrt{\frac{\Delta r_B r_{\text{DF},r}^2}{2r_{\text{DF},r} + \Delta r_B}} = \sqrt{\frac{r_{\text{DF},r}^2}{4Br_{\text{DF},r}/c + 1}} \quad (30)$$

with  $r_{\text{sr}} \leq r_{\text{DF},r}$ . Note that the size of the super-resolution region strongly depends on the system bandwidth. For a fixed number of antennas (and hence fixed  $r_{\text{DF},r}$ ), the wider the bandwidth, the smaller the super-resolution region.

Combining the DF in (28) with the definition of the super-resolution region in (30), the overall range resolution of the monostatic wideband NF sensing system as a function of the focusing distance  $\bar{r}$  can be written as<sup>6</sup>

$$\Delta r(\bar{r}) = \begin{cases} \frac{2\bar{r}^2 r_{\text{DF},r}}{r_{\text{DF},r}^2 - \bar{r}^2} & \bar{r} < r_{\text{sr}} \leq r_{\text{DF},r} \\ \Delta r_B = \frac{c}{2B} & \bar{r} \geq r_{\text{sr}}. \end{cases} \quad (31)$$

In other words, the range resolution is governed by NF beam focusing within the super-resolution region ( $\bar{r} < r_{\text{sr}}$ ), whereas it is limited by the bandwidth outside this region, even when focusing within the effective NF region, i.e.,  $\bar{r} < r_{\text{DF},r}$ .

From Fig. 4, we also observe that the bandwidth affects the range profile even when the target lies in the super-resolution region. In this regime, the main-lobe width is mainly governed by NF beam focusing, whereas the bandwidth helps suppress sidelobes in the overall range profile, especially near the edge of the super-resolution area [17]. Similarly, for focusing distances within the effective NF region but outside the super-resolution region, the range resolution is clearly determined by the bandwidth, while the NF array factor still contributes to significant sidelobe attenuation. This shows that, in a wideband NF sensing system, bandwidth and NF effects not only compete in setting the achievable range resolution,

<sup>6</sup>It is worth noting that the overall range resolution expression in (31) remains meaningful even though the two contributing terms are defined using different criteria (Rayleigh for  $\Delta r_B$  and half-power width for  $\text{DF}_r$ ). In fact, as shown in [39], when a rectangular transmit pulse  $g_{\text{tx}}(t)$  is used, the Rayleigh and half-power criteria yield approximately equivalent range resolutions.

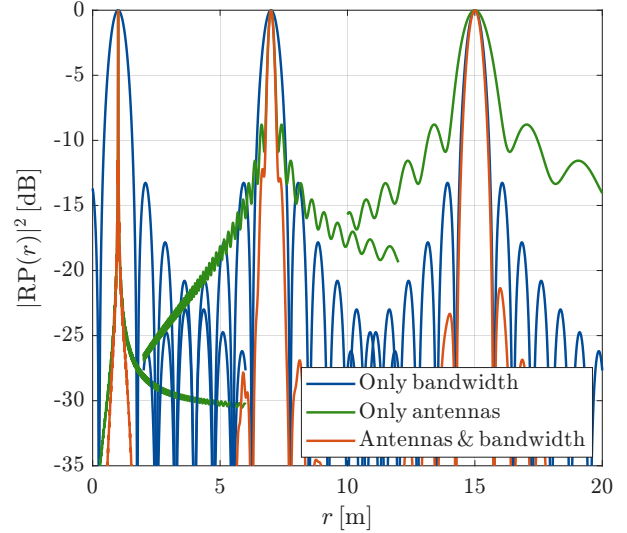


Figure 4: Range profile obtained focusing locations at different distances ( $\bar{r} = 1, 7, 15$  m) from the transceiver at  $\theta = 0^\circ$ . Note that, with  $f_c = 60$  GHz,  $B = 200$  MHz,  $K = 1024$ ,  $d_t = \lambda/2$ ,  $d_r = N_t \lambda/2$  and  $N_t = N_r = 32$ , the effective NF region and super-resolution area are limited by  $r_{\text{DF},r} = 376.1$  m and  $r_{\text{sr}} = 11.9$  m, respectively.

but also jointly improve the overall range profile by reducing the peak sidelobe level.

## V. TARGET PARAMETER DETECTION AND ESTIMATION

In this work, large-scale arrays are assumed at both Tx and Rx, so each beam pattern approximately forms a narrow lobe around a steering direction  $\theta$ . Referring to the system model of Section II, we adopt a conventional transmit beamforming vector  $\mathbf{w}_t = \mathbf{a}(\theta)/\|\mathbf{a}(\theta)\|$ . From the Rx perspective, the effective channel from the Tx to a generic micro-scatterer  $p$  of the ET is then modulated by the complex beamforming gain  $g_p \triangleq \mathbf{a}^H(\theta_p)\mathbf{w}_t$ , which captures the alignment between the scatterer AoD  $\theta_p$  and the current transmit beam. For notational convenience, this gain is absorbed into the complex channel coefficient as  $h_p \triangleq g_p \epsilon_p$ , so that, unlike (6), the received signal model is expressed in terms of  $h_p$  rather than  $\epsilon_p$ .

For later processing, it is convenient to rewrite the received signal in (5) in vector form as  $\mathbf{y} \in \mathbb{C}^{N_r KM \times 1}$  by stacking the samples across subcarriers, OFDM symbols, and antennas

$$\mathbf{y} = \sum_{p=1}^P \sqrt{\frac{P_t G_t G_r}{K}} h_p \mathbf{G}(r_p, \tau_p, \theta_p, f_{D,p}) \mathbf{x} + \mathbf{v} \quad (32)$$

where  $\mathbf{x} \in \mathbb{C}^{KM \times 1}$  stacks the transmitted symbols  $x[k, m]$ ,  $\mathbf{v} \in \mathbb{C}^{N_r KM \times 1}$  stacks the AWGN samples  $v_n[k, m]$ , and  $\mathbf{G}(\cdot) \in \mathbb{C}^{N_r KM \times KM}$  is the effective channel matrix for scatterer  $p$ , defined as

$$\mathbf{G}(r_p, \tau_p, \theta_p, f_{D,p}) \triangleq \mathbf{T}(\tau_p, f_{D,p}) \otimes \mathbf{b}(\theta_p, r_p) \quad (33)$$

with

$$\begin{aligned} \mathbf{T}(\tau_p, f_{D,p}) \triangleq \text{diag} \left( [1, \dots, e^{j2\pi(M-1)T_s f_{D,p}}]^T \otimes \right. \\ \left. \otimes [1, \dots, e^{-j2\pi(K-1)\Delta f \tau_p}]^T \right) \end{aligned} \quad (34)$$

a diagonal matrix of size  $KM \times KM$ . Since the two-way propagation delay of scatterer  $p$  satisfies  $\tau_p = 2r_p/c$ , we can equivalently write  $\mathbf{T}(\tau_p, f_{D,p}) \equiv \mathbf{T}(r_p, f_{D,p})$  and, correspondingly,  $\mathbf{G}(r_p, \tau_p, \theta_p, f_{D,p}) \equiv \mathbf{G}(r_p, \theta_p, f_{D,p})$ .

For an ET with  $P$  micro-scatterers, the unknown parameter set is  $\Theta = \{\Theta_p\}_{p=1}^P$ , where  $\Theta_p = \{|h_p|, \angle h_p, r_p, \theta_p, f_{D,p}\}$ . The joint maximum likelihood (ML) estimate involves a search over  $\Gamma \triangleq \mathbb{C}^P \times \mathbb{R}^{3P}$  [23]

$$\Theta_{\text{ML}} = \arg \min_{\Theta \in \Gamma} \left\| \mathbf{y} - \sum_{p=1}^P \sqrt{\frac{P_t G_t G_r}{K}} h_p \mathbf{G}(r_p, \theta_p, f_{D,p}) \mathbf{x} \right\|^2. \quad (35)$$

However, solving (35) would require knowledge of the number of scatterers  $P$  and leads to a high-dimensional model-order selection problem [40], which is intrinsically ill-posed for ETs with many indistinguishable micro-scatterers [41]. Following the grid-based GLRT framework adopted in [23], we instead consider a discrete search grid  $\Psi$  over  $(r, \theta, f_D)$  and assume that at most one micro-scatterer can lie in each grid cell.

Starting from the likelihood associated with (35) and substituting the ML estimate of the complex gain  $h_p$  (see [23, eq. (41)]), the resulting GLRT metric for a candidate triplet  $(r, \theta, f_D) \in \Psi$  can be written as

$$\ell(r, \theta, f_D) = \frac{|\boldsymbol{\xi}(r, f_D) \mathbf{b}^*(\theta, r)|^2}{\mathbf{x}^H \mathbf{b}^H(\theta, r) \mathbf{b}(\theta, r) \mathbf{x}} \stackrel{\mathcal{H}_1}{\geq} \eta \quad (36)$$

with  $\boldsymbol{\xi}(r, f_D) = \mathbf{x}^H \mathbf{T}^H(r, f_D) \mathbf{Y}^T$  and  $\mathbf{Y} = [\mathbf{y}[0, 0], \dots, \mathbf{y}[M-1, K-1]] \in \mathbb{C}^{N_r \times KM}$  obtained by stacking the received vectors in (5) over all subcarriers and OFDM symbols.

In (36), a binary hypothesis test is performed to decide whether the cell contains a micro-scatterer ( $\mathcal{H}_1$ ) or not ( $\mathcal{H}_0$ ) with the threshold  $\eta$  chosen to guarantee a given false alarm rate (FAR). Under  $\mathcal{H}_0$ , when only noise is present at the receiver (i.e.,  $\mathbf{y} = \boldsymbol{\nu}$ ), the statistic  $\ell(r, \theta, f_D)$  is exponentially distributed with mean  $\sigma_{\nu}^2$ . Hence, for a desired per-bin false-alarm probability  $P_{\text{FA,point}}$ , the threshold is

$$\eta = -\sigma_{\nu}^2 \ln(P_{\text{FA,point}}). \quad (37)$$

To guarantee a given FAR over the entire search grid  $\Psi$  with  $\text{card}(\Psi)$  points, we set  $P_{\text{FA,point}} = \text{FAR}/\text{card}(\Psi)$ .

The outcome of the procedure in (36) is a *radar image* in the  $(r, \theta, f_D)$  space, where localized peaks of  $\ell(r, \theta, f_D)$  correspond to dominant scattering points of the ET, in line with the interpretation in [23]. In practice, this radar map is obtained through a coordinated beam-scanning procedure. The Tx beam is steered over a discrete set of  $N_d$  directions  $\{\bar{\theta}_q\}_{q=0}^{N_d-1}$  that cover a given region of interest (RoI). For each direction  $\bar{\theta}_q$ , the transmit beamforming vector is set to  $\mathbf{w}_t = \mathbf{a}(\bar{\theta}_q)$ , and the Rx performs beam focusing within the corresponding beamspace sector according to the NF steering vector  $\mathbf{b}(\theta, r)$  used in (36). The scan step is chosen on the order of the 3 dB beamwidth of the Tx array,  $\Delta\theta_{3\text{dB}}^{\text{tx}} \approx 2/N_t$  (in radians), so that adjacent beams overlap and jointly cover the RoI. Since the Tx and Rx arrays are co-located, this transmit–receive scanning can be naturally synchronized, and

TABLE I

Simulation parameters		
$f_c$	Carrier frequency	60 GHz
$K$	Active subcarriers for sensing	1024
$M$	OFDM symbols	10
$N_t / N_r$	Number of Tx / Rx antennas	32
$D_t$	Tx aperture array	0.08 m
$D_r$	Rx aperture array	2.48 m
$G_t / G_r$	Tx / Rx antenna element gain	1
$\text{EIRP} \triangleq P_t G_t N_t$	Equivalent isotropic radiated power	0.1 W
$n_F$	Receiver noise figure	10 dB
$\sigma_p = \sigma$	Micro-scatterer RCS	0.25 m <sup>2</sup>
$A_{\text{RoI}}$	RoI area	$3 \times 3$ m <sup>2</sup>
$D_{\text{F}}^{\text{tx}}$	Tx Fraunhofer distance	2.4 m
$D_{\text{F}}^{\text{rx}}$	Rx Fraunhofer distance	2460 m
$L / W$	ET length / width	2 m / 1 m
$q$	ET grid scatterer probability	0.1
$ \mathcal{E} $	Number of ET grid elements	200
FAR	Expected number of false-alarm bins per map	1
$N_{\text{MC}}$	Monte Carlo iterations	1000

the GLRT metric in (36) is evaluated for all  $(r, \theta, f_D)$  grid points illuminated by each beam. After all  $N_d$  beams have been processed, the collection of GLRT values forms a radar map over the RoI. For a more comprehensive explanation, readers can refer to [42].

Finally, once the range–angle pair  $(\hat{r}_p, \hat{\theta}_p)$  of each detected micro-scatterer is estimated from the grid, its Cartesian position is obtained as

$$\hat{\mathbf{p}}_p = [\hat{x}_p, \hat{y}_p]^T = [\hat{r}_p \cos(\hat{\theta}_p), \hat{r}_p \sin(\hat{\theta}_p)]^T. \quad (38)$$

## VI. NUMERICAL RESULTS

Numerical simulations are performed to evaluate the effectiveness of the proposed ELAS method and to quantify how the enhanced NF range resolution impacts the position-estimation accuracy of the scatterers of an ET in a wideband OFDM-based monostatic sensing system. The target moves inside a monitored area of size  $20 \times 20$  m<sup>2</sup>, as shown in Fig. 5, where the white stars labeled 1, 2, and 3 mark the centroids of the rectangular ET in the three simulation setups. In particular, the ET centroid is placed at  $\mathbf{p}_0 = [5, 3]^T$  and  $\mathbf{p}_0 = [3.5, 0]^T$  in configurations 1 and 2, with tangential and normal headings with respect to the array, respectively, and at  $\mathbf{p}_0 = [17, -8]^T$  in configuration 3, where it is also normally oriented.

First, we show that the angle ambiguities caused by the large inter-element spacing at the Rx can be naturally avoided when the transmit–receive spacing prescribed by ELAS is adopted. Then, we assess localization performance by computing the GOSPA metric over the ET scatterers and the RMSE of the estimated ET centroid.

The simulations consider the system parameters in Table I and the quadrature phase shift keying (QPSK) constellation for each subcarrier, while the system bandwidth  $B$  is varied in the range 50–750 MHz to investigate its effect on localization resolution and accuracy in wideband NF sensing. As  $B$  changes, the subcarrier spacing  $\Delta f$  (and hence the OFDM symbol duration  $T_s$ ) is adjusted accordingly to keep the number of active subcarriers fixed as per Table I. Notably, with the proposed ELAS design and  $N_t = N_r = 32$  antennas at both Tx and Rx, we obtain a large Fraunhofer distance  $D_{\text{F}}^{\text{rx}} = 2460$  m and an effective maximum focusing distance

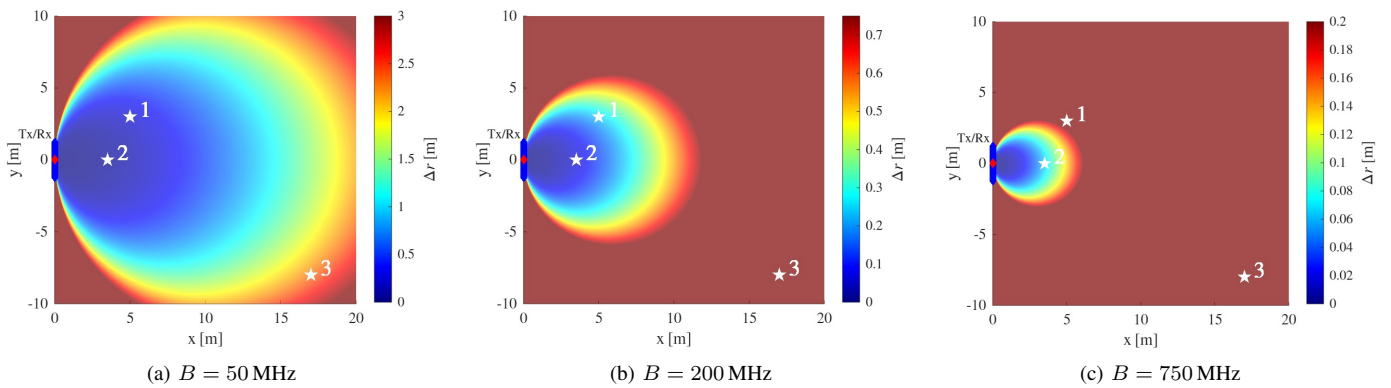


Figure 5: Range-resolution map  $\Delta r(x, y)$  over the monitored area for (a)  $B = 50$  MHz, (b)  $B = 200$  MHz, and (c)  $B = 750$  MHz by using the ELAS design with  $f_c = 60$  GHz and  $N_t = N_r = 32$ . These maps illustrate how the super-resolution region (low  $\Delta r$  area) shrinks as the bandwidth increases. White stars labelled 1–3 indicate the ET centroid positions for the three simulation setups: (1)  $\mathbf{p}_0 = [5, 3]^T$ , (2)  $\mathbf{p}_0 = [3.5, 0]^T$ , and (3)  $\mathbf{p}_0 = [17, -8]^T$ .

$r_{\text{DF},r} \approx 376$  m at the Rx, thus achieving an extended NF region with a relatively small number of elements. The impact of this maximum focusing distance on the overall system range resolution for different bandwidths is analyzed in detail in the next subsection.

#### A. Range Resolution of Wideband Near-Field Sensing

Fig. 5 shows the resulting range-resolution map  $\Delta r(x, y)$  over the monitored area for three bandwidth values,  $B = \{50, 200, 750\}$  MHz, obtained from (31). As mentioned above, this area is entirely contained within the effective NF region of the Rx, since  $r_{\text{DF},r} \approx 376$  m for the parameters in Table I. The plots clearly highlight two regimes: (i) a central super-resolution region, where  $\Delta r(x, y)$  is dominated by the DF term  $\text{DF}_r(\bar{\mathbf{r}})$  and can be significantly smaller than the bandwidth-limited resolution  $\Delta r_B$ , and (ii) an outer region where the range resolution is essentially flat and equal to  $\Delta r_B$ .

As the bandwidth decreases, the super-resolution region expands towards the edge of the monitored area, so that for  $B = 50$  MHz it covers almost the entire  $20 \times 20 \text{ m}^2$  domain. In this regime, when the system bandwidth is limited, NF beam focusing becomes the dominant driver of range resolution. Conversely, for larger bandwidths (e.g.,  $B = 750$  MHz), the super-resolution region shrinks to a small neighborhood around the array. In this case, the overall range resolution is predominantly set by  $\Delta r_B$  over most of the monitored area, although the entire area still lies within the effective NF region defined by  $r_{\text{DF},r}$ . This confirms that, in wideband NF sensing, the DF alone is not sufficient to improve range resolution beyond the bandwidth limit; NF gains are realized only within the super-resolution region, whose spatial extent is governed by both  $B$  and  $r_{\text{DF},r}$  according to (30).

For a fixed bandwidth, the size of the super-resolution region grows with  $r_{\text{DF},r}$  and thus with the aperture of the receive ELAA. With the proposed ELAS design, we choose  $d_r = N_t \lambda / 2$  and  $d_t = \lambda / 2$ , so that the effective aperture of the Rx is on the order of  $N_r N_t \lambda / 2$ , while only  $N_r$  physical elements are used. In contrast, a conventional  $\lambda / 2$ -spaced ELAA would need approximately  $N_t N_r$  elements to achieve a comparable aperture. Therefore, ELAS achieves a large  $r_{\text{DF},r}$ , resulting in a wide super-resolution region, while reducing the number

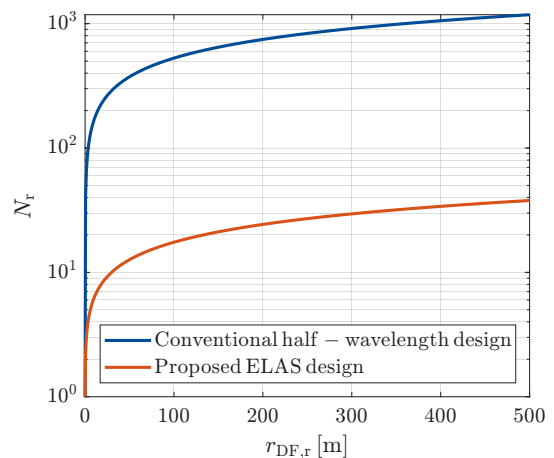


Figure 6: Comparison of the number of Rx antenna elements required to achieve a target maximum focusing distance  $r_{\text{DF},r}$  for the proposed ELAS architecture and a conventional half-wavelength-spaced array, with  $f_c = 60$  GHz and  $N_t = 32$ .

of antennas and RF chains by approximately a factor of  $N_t$ , as can be seen in Fig. 6. This approach significantly lowers system complexity and power consumption, yet preserves the NF range-resolution gain.

#### B. Impact of the Enhanced Wideband Near-Field Range Resolution on ET Position Estimation Accuracy

In general, range resolution and localization accuracy are distinct performance metrics: the former quantifies the ability to separate closely spaced scatterers, whereas the latter measures how close the estimated positions are to their true locations. For ETs, however, these metrics are strongly coupled: as the radar range resolution improves, more scattering contributions from the ET can be individually resolved, providing richer spatial information. In this sense, higher resolution not only refines the structural representation of the target but also tends to improve the accuracy of its geometric center.

To quantify this effect, we simulate a wideband NF OFDM-based ISAC system with an ET located in configurations 1, 2, and 3 of Fig. 5, using  $N_{\text{MC}} = 1000$  Monte Carlo trials. As discussed in Section V, target parameter estimation is

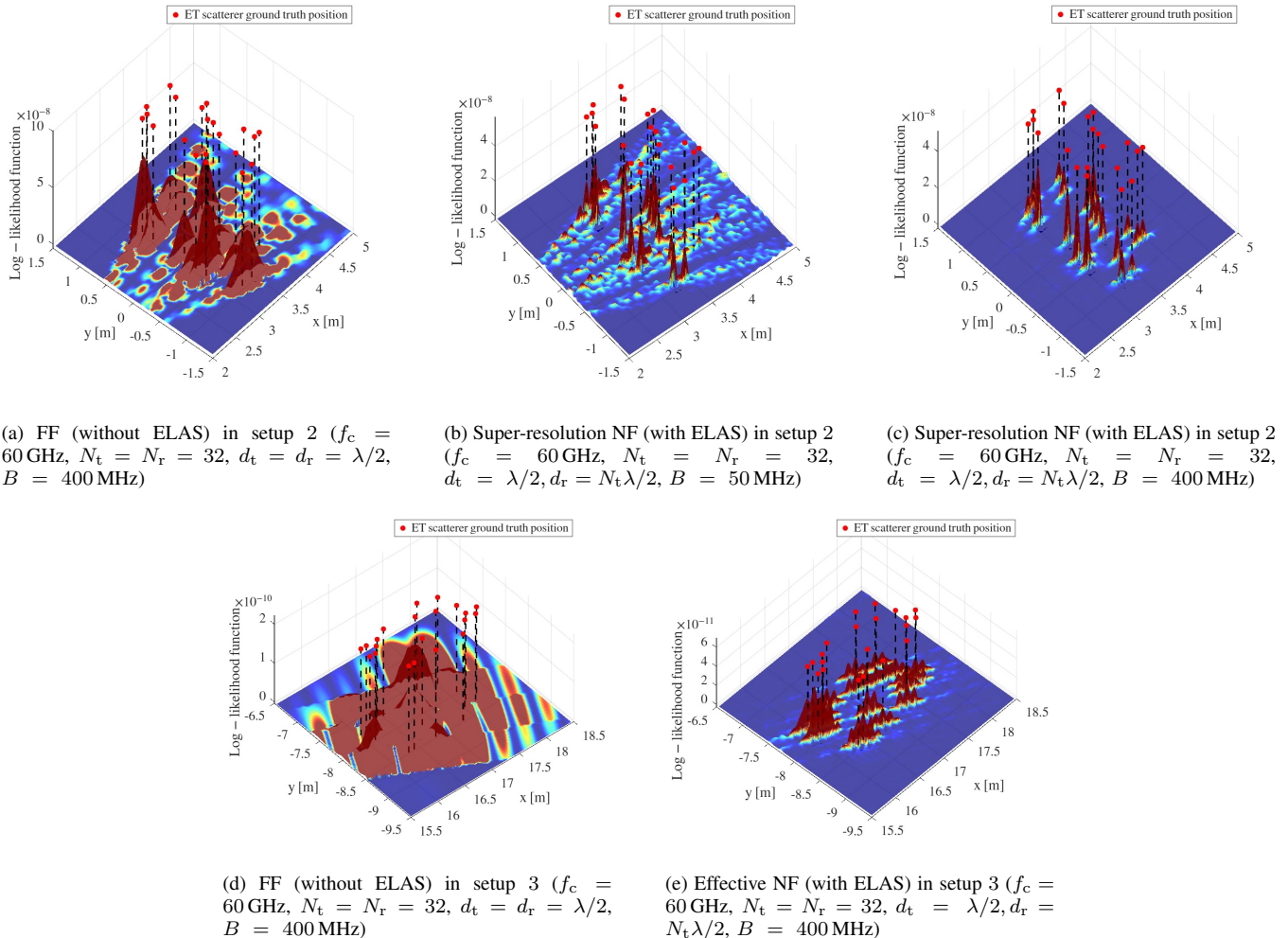


Figure 7: Log-likelihood profile within the search RoI for different simulation setups and system bandwidths, evaluated under both FF conditions with the conventional half-wavelength spacing at both Tx and Rx, and effective NF propagation enabled by the proposed ELAS method.

performed over a RoI of size  $3 \times 3$  m<sup>2</sup> centered at the true centroid position  $\mathbf{p}_0$  of the ET. The GLRT detector in (36) is employed for joint detection and estimation, with the threshold set according to (37) to guarantee a total FAR per radar map equal to  $\text{FAR} = 1$ , i.e., on average one noise-only pixel exceeding the threshold per map.

In this work, we focus on a stationary ET, so its Doppler shift is identically zero over the measurement interval. Accordingly, in the GLRT of (36), we fix the Doppler to its true value,  $f_D = 0$  Hz, and evaluate the metric over a two-dimensional grid in  $(r, \theta)$ :  $\ell(r, \theta) \triangleq \ell(r, \theta, f_D=0)$ . This reduces the problem dimensionality by treating the Doppler as a known part of the model (i.e., static target hypothesis). Moreover, in the considered setup, only  $M = 10$  OFDM symbols are available, so the Doppler resolution  $1/(MT_s)$  is relatively coarse and would not allow reliable discrimination between a slowly moving ET and static objects based on Doppler information alone. In fact, as shown in [42] for a similar setting, using  $f_D = 0$  Hz as a reference Doppler value yields a negligible impact on localization performance even for slowly moving targets, while significantly reducing the computational burden compared to a full 3-dimensional search.

The radar map in the Cartesian  $x$ - $y$  domain is obtained by evaluating  $\ell(r, \theta)$  on a polar grid within the RoI, applying the GLRT detector in (36), and mapping each grid point  $(r, \theta)$  to  $(x, y)$  via the polar-to-Cartesian transformation in (38). As illustrated in Fig. 7, the resulting maps exhibit multiple local peaks in the  $x$ - $y$  plane. While some peaks may arise from sidelobes, most are expected to correspond to effective scattering points of the ET. The peak locations thus provide estimates of the micro-scatterer positions. To refine detection, a peak-picking procedure is applied to the map so that only local maxima of  $\ell(r, \theta)$  are retained as detected points, rather than using the full GLRT profile.

The performed simulations analyze how the enhanced range resolution produced by the joint effect of bandwidth and NF propagation impacts ET localization, both inside and outside the super-resolution region. To this end, we evaluate two localization metrics as functions of the system bandwidth  $B$ .

The first metric is the RMSE of the ET scattering centroid estimation, whose ground-truth value for the  $i$ -th iteration is defined as the barycenter of the scatterer positions  $\bar{\mathbf{p}}_0^i \triangleq (1/P^{(i)}) \sum_{p=1}^{P^{(i)}} \mathbf{p}_p$ , where  $P^{(i)}$  is the number of ET scatterers

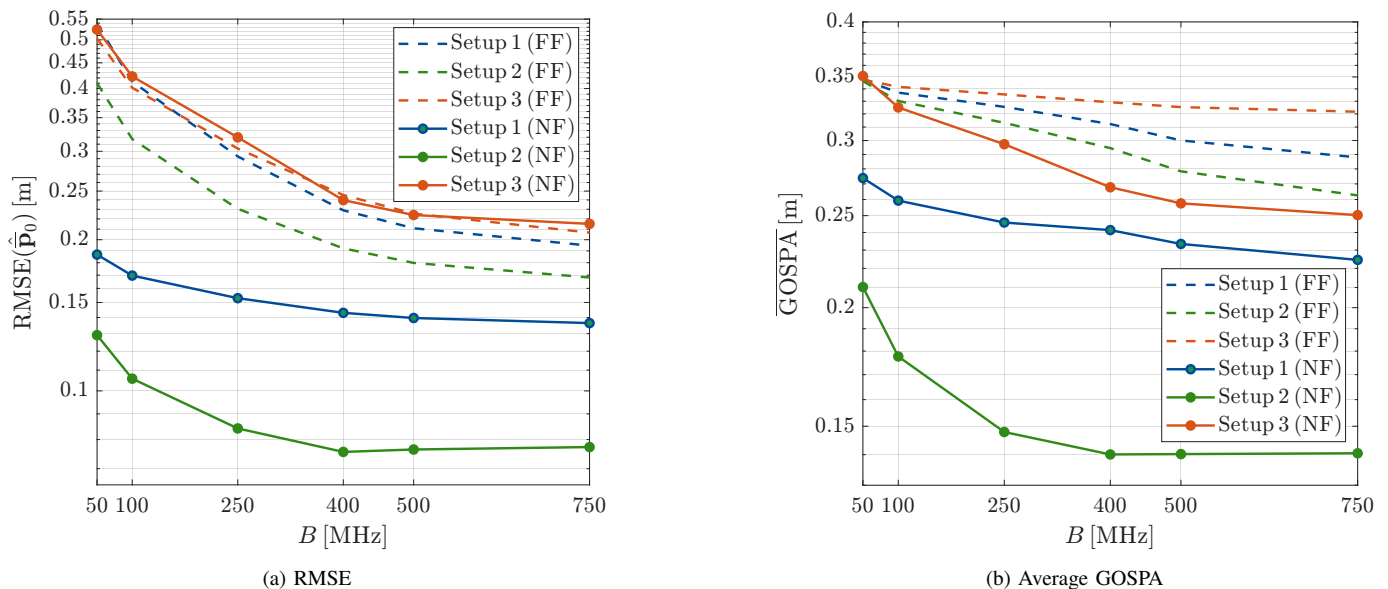


Figure 8: Localization performance as a function of the system bandwidth  $B$  with  $N_t = N_r = 32$  antennas, in FF conditions with conventional half-wavelength spacing ( $d_t = d_r = \lambda/2$ ) and in the effective NF of the Rx enabled by the proposed ELAS method ( $d_t = \lambda/2$ ,  $d_r = N_t \lambda/2$ ). (a) RMSE of ET scattering centroid position  $\hat{\mathbf{p}}_0$ ; (b) average GOSPA over the detected scatterers.

at a given Monte Carlo run  $i$ . The corresponding RMSE is

$$\text{RMSE}(\hat{\mathbf{p}}_0) = \sqrt{\frac{1}{N_{\text{MC}}} \sum_{i=1}^{N_{\text{MC}}} \|\hat{\mathbf{p}}_0^i - \bar{\mathbf{p}}_0\|^2}$$

where  $\bar{\mathbf{p}}_0^i$  and  $\hat{\mathbf{p}}_0^i$  are the true and estimated centroids at the  $i$ -th trial, respectively. This metric reflects both the ability to resolve multiple scattering points and the accuracy of their position estimates.

As a second metric, we use the GOSPA distance [43], widely adopted in multi-target and multi-scatterer localization. GOSPA compactly captures localization error, missed detections, and false alarms in a single scalar score. We adopt the standard GOSPA formulation as per [44, Eq. (12)], with gating parameter  $\xi_g = 0.5$  m (chosen to be on the order of five times the grid spacing, i.e., the distance between two adjacent pixels in the RoI), and order  $q = 2$ , and compute the average GOSPA over  $N_{\text{MC}}$  trials. In particular, estimated scatterers farther than  $\xi_g$  from any true scatterer are treated as false alarms, and true scatterers without an estimate within  $\xi_g$  are counted as missed detections. A lower GOSPA value indicates better overall ET localization performance.

The impact of NF operation is assessed by comparing it with a FF baseline under the simulation parameters in Table I. As a FF baseline, we consider conventional half-wavelength ULAs at both the Tx and Rx, while as an NF alternative, we employ the proposed ELAS design, so that the ET lies in the effective NF region of the Rx.

Fig. 7 illustrates the GLRT-based radar maps for representative cases. In Fig. 7b and Fig. 7c, corresponding to setup 2 of Fig. 5, i.e., with the ET in the NF super-resolution region, the proposed ELAS spacing yields ambiguity-free angle profiles despite the large inter-element spacing at the Rx. Comparing the FF profile in Fig. 7a (half-wavelength arrays

at both ends) with the NF profile in Fig. 7c for the same bandwidth  $B = 400$  MHz, we clearly observe the enhanced range resolution enabled by NF operation, with the scattering contributions from the ET much more finely separated than the FF case. Moreover, as discussed in Section IV, bandwidth still plays a key role even within the super-resolution region. The comparison between Fig. 7b and Fig. 7c shows that increasing  $B$  substantially suppresses sidelobes in the range profile, yielding a cleaner overall radar image. The interplay between bandwidth and NF beam focusing is also observed outside the super-resolution region, as outlined in Section IV. In this regime, although the range resolution is primarily determined by the signal bandwidth, operating under effective NF conditions produces a cleaner range response, i.e., with lower sidelobe levels. Moreover, the larger physical antenna aperture improves the angular resolution. This is evident by comparing the GLRT-based radar maps in Fig. 7d and Fig. 7e, when the ET is outside the super-resolution region in the simulation setup 3 of Fig. 5.

Fig. 8a shows the RMSE of the ET centroid as a function of  $B$  for the three target setups. In the FF case, the behavior isolates the effect of bandwidth alone. For all setups, increasing  $B$  (i.e., improving bandwidth-limited range resolution) leads to a marked reduction of the RMSE, with additional gains when the ET is closer to the transceiver due to a higher signal-to-noise ratio (SNR). In the NF case, a similar trend with  $B$  is visible in setup 3, where the ET remains outside the super-resolution region for all considered bandwidths (with the only exception at  $B = 50$  MHz, where the ET lies close to the boundary of the super-resolution region). Here, the range resolution is dominated by  $\Delta r_B$ , and the NF and FF RMSE curves nearly overlap. This confirms that, when the target lies in the effective NF region but outside the super-resolution region, localization accuracy is still essentially governed by the bandwidth-induced range resolution.

Conversely, in setups 1 and 2, where the ET lies inside the super-resolution region for almost the entire bandwidth interval, the centroid RMSE remains nearly constant with respect to  $B$ . In this regime, the range resolution is dominated by the NF contribution and is essentially independent of the bandwidth. Increasing  $B$  therefore does not further improve the resolution, except for  $B \lesssim 400$  MHz, where a larger bandwidth helps suppress sidelobes in the range profile and yields a modest RMSE reduction, in line with the discussion in Section IV. Overall, within the super-resolution region, the NF-enhanced range resolution yields a substantial RMSE gain over the FF baseline, especially for limited bandwidths. Moreover, since the NF range resolution is range-dependent, setup 2 (with the ET closer to the array and higher SNR) benefits from finer effective resolution than setup 1 (see Fig. 5), which translates into improved centroid accuracy.

Fig. 8b shows the average GOSPA for all setups in both FF and NF conditions. As with the RMSE, increasing  $B$  and placing the ET closer to the array generally improves the metric thanks to higher SNR and finer range resolution when the target lies in the super-resolution NF region. In the FF case, the trend mirrors that of Fig. 8a since performance is solely driven by bandwidth-limited resolution. This means that a larger  $B$  allows for better discrimination of closely spaced scatterers, reducing both localization error and misdetections.

Unlike the centroid RMSE, NF operations yield lower GOSPAs than FF across all setups. Notably, even in setup 3, where the ET lies outside the super-resolution region, GOSPA improves significantly under NF conditions, although the nominal range resolution remains bandwidth-limited as in FF. This improvement is due to additional range–angle focusing beyond pure angle-domain beam steering as well as sidelobe reduction in the range profile (see Section IV), to which GOSPA is particularly sensitive due to sidelobe-induced false alarms. As the bandwidth  $B$  increases, the higher range resolution reduces GOSPA under both FF and NF, mirroring the RMSE trend. However, the decrease is more pronounced in the NF setup, as improved resolution combined with NF-driven sidelobe mitigation further reduces false alarms.

## VII. CONCLUSIONS

In this work, we proposed a monostatic wideband MIMO OFDM-based ISAC system at mmWave frequencies operating under hybrid near-/far-field conditions: the Tx is designed to work in the FF with low-complexity beam steering, while the Rx operates in the NF by means of an ELAA. The latter is realized as a ULA designed according to an ELAS design method, which enlarges the effective aperture by appropriately spacing the receive elements beyond half a wavelength without introducing angle ambiguities. This extends the Fraunhofer distance and enables NF sensing gains in spatial resolution and localization accuracy, while remaining compatible with a low-complexity fully digital architecture with only a few RF chains. In addition, we analyzed the range resolution of wideband NF sensing and identified a super-resolution region where NF effects enhance the achievable range resolution beyond the classical bandwidth limit.

Numerical results validate the ability of the ELAS design to create effective NF conditions with only tens of antenna elements at both ends of the link while naturally avoiding angle ambiguities. Furthermore, we demonstrate that for ET modeled as a collection of scatterers, the enhanced NF range resolution within the super-resolution region improves localization accuracy, as measured by the RMSE of the estimated target scattering centroid. Finally, although NF effects dominate range resolution inside the super-resolution region, waveform bandwidth still plays a key role in shaping the range profile. Moreover, outside this region—where range resolution is bandwidth-limited—the interplay between bandwidth and NF effects reduces range sidelobe levels, mitigating sidelobe-induced false alarms, in agreement with the consistently lower GOSPA values observed under NF. Overall, the proposed ELAS-enabled architecture provides a practical approach for exploiting NF super-resolution in wideband sensing with moderate array sizes and fully digital processing.

## REFERENCES

- [1] Y. Liu, Z. Wang, J. Xu, C. Ouyang, X. Mu, and R. Schober, “Near-field communications: A tutorial review,” *IEEE Open J. Commun. Soc.*, vol. 4, pp. 1999–2049, Aug. 2023.
- [2] A. Carfagna and S. Bartoletti, “Power split optimization for joint communication and sensing in MIMO OFDM systems,” *IEEE Wireless Commun. Lett.*, vol. 15, pp. 655–659, 2026.
- [3] Z. Wang, P. Ramezani, Y. Liu, and E. Björnson, “Near-field localization and sensing with large-aperture arrays: From signal modeling to processing,” *IEEE Signal Process. Mag.*, vol. 42, no. 1, pp. 74–87, Jan. 2025.
- [4] M. Cui and L. Dai, “Channel estimation for extremely large-scale MIMO: Far-field or near-field?” *IEEE Trans. Commun.*, vol. 70, no. 4, pp. 2663–2677, Apr. 2022.
- [5] C. Giovannetti, T. Bacchielli, A. Giorgetti, D. Dardari, and N. Decarli, “Error bound analysis for velocity estimation in near-field bistatic radar systems,” *IEEE Trans. Aerosp. Electron. Syst.*, pp. 1–18, 2025.
- [6] Q. Dai, Y. Zeng, H. Wang, C. You, C. Zhou, H. Cheng, X. Xu, S. Jin, A. Lee Swindlehurst, Y. C. Eldar, R. Schober, R. Zhang, and X. You, “A tutorial on MIMO-OFDM ISAC: From far-field to near-field,” *IEEE Commun. Surveys Tuts.*, vol. 28, pp. 4319–4358, Jan. 2026.
- [7] Z. He, W. Xu, Z. Yang, H. Shen, N. Fu, Y. Huang, Z. Zhang, and X. You, “Unlocking potentials of near-field propagation: ELAA-empowered integrated sensing and communication,” *IEEE Commun. Mag.*, vol. 62, no. 9, pp. 82–89, Sep. 2024.
- [8] J. Cong, C. You, J. Li, L. Chen, B. Zheng, Y. Liu, W. Wu, Y. Gong, S. Jin, and R. Zhang, “Near-field integrated sensing and communication: Opportunities and challenges,” *IEEE Wireless Commun.*, vol. 31, no. 6, pp. 162–169, Dec. 2024.
- [9] B. Sambon, F. De Saint Moulin, G. Thiran, C. Oestges, and L. Vandendorpe, “Electromagnetic modeling of extended targets in a distributed antenna system,” *IEEE Trans. Rad. Syst.*, vol. 3, pp. 1257–1268, Sep. 2025.
- [10] A. Kosasih, O. T. Demir, N. Kolomvakis, and E. Björnson, “Spatial frequencies and degrees of freedom: Their roles in near-field communications,” *IEEE Signal Process. Mag.*, vol. 42, no. 1, pp. 33–44, Jan. 2025.
- [11] D. T. Bellini, D. Tagliaferri, M. Mizmizi, S. Tebaldini, and U. Spagnolini, “Multi-view near-field imaging in NLOS with non-reconfigurable EM skins,” in *IEEE Int. Conf. on Comm. Works. (ICC Workshops)*, 2024, pp. 384–389.
- [12] A. Dürr, B. Schneele, D. Schwarz, and C. Waldschmidt, “Range-angle coupling and near-field effects of very large arrays in mm-Wave imaging radars,” *IEEE Trans. Microw. Theory Techn.*, vol. 69, no. 1, pp. 262–270, Jan. 2021.
- [13] E. Björnson, O. T. Demir, and L. Sanguinetti, “A primer on near-field beamforming for arrays and reconfigurable intelligent surfaces,” in *Proc. 55th Asilomar Conf. Signals Syst. Comput.*, Pacific Grove, CA, USA, Oct. 2021, pp. 105–112.

- [14] A. Kosasih and E. Björnson, "Finite beam depth analysis for large arrays," *IEEE Trans. Wireless Commun.*, vol. 23, no. 8, pp. 10015–10029, Aug. 2024.
- [15] M. Wachowiak, A. Bourdoux, and S. Pollin, "Analysis of the ambiguity function of narrowband near-field MIMO radar," Jul. 2025. [Online]. Available: <https://arxiv.org/abs/2505.10053>
- [16] Z. Wang, X. Mu, and Y. Liu, "Rethinking integrated sensing and communication: When near field meets wideband," *IEEE Commun. Mag.*, vol. 62, no. 9, pp. 44–50, Sep. 2024.
- [17] M. Wachowiak, A. Bourdoux, and S. Pollin, "Approximation of the range ambiguity function in near-field sensing systems," *IEEE Trans. Rad. Syst.*, pp. 1–1, early access, Jan. 2026.
- [18] M. Rahal, A. Elzanaty, M. Mirmohseni, and Y. Ma, "Near-field wideband OFDM ISAC: Sensing algorithm and precoding design," in *Proc. IEEE Int. Conf. Commun. (ICC)*, Montreal, QC, Canada, Jun. 2025, pp. 3936–3941.
- [19] M. Rahal, A. Elzanaty, M. Mirmohseni, Y. Ma, and R. Tafazolli, "Near-field wideband ISAC: Estimator design and performance analysis," *IEEE Trans. Aerosp. Electron. Syst.*, pp. 1–14, early access, Sep. 2025, doi:10.1109/TAES.2025.3605909.
- [20] X. Wang, W. Zhai, X. Wang, M. G. Amin, and K. Cai, "Wideband near-field integrated sensing and communication with sparse transceiver design," *IEEE J. Sel. Topics Signal Process.*, vol. 18, no. 4, pp. 662–677, May 2024.
- [21] Z. Wang, X. Mu, and Y. Liu, "Performance analysis of near-field sensing in wideband MIMO systems," *IEEE Trans. Wireless Commun.*, vol. 24, no. 10, pp. 8236–8251, Oct. 2025.
- [22] H. Lu, Y. Zeng, C. You, Y. Han, J. Zhang, Z. Wang, Z. Dong, S. Jin, C.-X. Wang, T. Jiang, X. You, and R. Zhang, "A tutorial on near-field XL-MIMO communications toward 6G," *IEEE Commun. Surveys Tuts.*, vol. 26, no. 4, pp. 2213–2257, Fourthquarter 2024.
- [23] S. K. Dehkordi, L. Pucci, P. Jung, A. Giorgetti, E. Paolini, and G. Caire, "Multistatic parameter estimation in the near/far field for integrated sensing and communication," *IEEE Trans. Wireless Commun.*, vol. 23, no. 12, pp. 17929–17944, Dec. 2024.
- [24] L. Pucci, S. K. Dehkordi, P. Jung, E. Paolini, A. Giorgetti, and G. Caire, "Performance analysis of multistatic integrated sensing and communication in the near/far field," in *Proc. IEEE Int. Symp. Pers. Indoor Mob. Radio Commun. (PIMRC)*, Valencia, Spain, Sep. 2024.
- [25] C. Meng, D. Ma, Z. Wang, Y. Liu, Z. Wei, and Z. Feng, "Near-field hybrid beamforming design for modular XL-MIMO ISAC systems," *IEEE Trans. Commun.*, vol. 73, no. 11, pp. 11 840 – 11 854, Nov. 2025.
- [26] J. Luo, J. Fan, and Y. Liu, "Beam focusing for near-field integrated sensing and communications with hybrid analog/digital architecture," *IEEE Trans. Wireless Commun.*, vol. 24, no. 10, pp. 8162–8177, Oct. 2025.
- [27] F. Liu and C. Masouros, "Hybrid beamforming with sub-arrayed MIMO radar: Enabling joint sensing and communication at mmWave band," in *Proc. IEEE Int. Conf. Acoust. Speech Signal Process. (ICASSP)*, Brighton, UK, May 2019, pp. 7770–7774.
- [28] X. Zhu, Y. Liu, and C.-X. Wang, "Sub-array-based millimeter wave massive MIMO channel estimation," *IEEE Wireless Commun. Lett.*, vol. 12, no. 9, pp. 1608–1612, Sep. 2023.
- [29] K. Qu, S. Guo, N. Saeed, and J. Ye, "Near-field integrated sensing and communication: Performance analysis and beamforming design," *IEEE Open J. Commun. Soc.*, vol. 5, pp. 6353–6366, Sep. 2024.
- [30] S. Ye, M. Xiao, M.-W. Kwan, Z. Ma, Y. Huang, G. Karagiannidis, and P. Fan, "Extremely large aperture array (ELAA) communications: Foundations, research advances and challenges," *IEEE Open J. Commun. Soc.*, vol. 5, pp. 7075–7120, Oct. 2024.
- [31] B. Friedlander, "On transmit beamforming for MIMO radar," *IEEE Trans. Aerosp. Electron. Syst.*, vol. 48, no. 4, pp. 3376–3388, Oct. 2012.
- [32] C. Baquero Barneto, T. Riihonen, M. Turunen, L. Anttila, M. Fleischer, K. Stadius, J. Ryyänen, and M. Valkama, "Full-duplex OFDM radar with LTE and 5G NR waveforms: Challenges, solutions, and measurements," *IEEE Trans. Microw. Theory Techn.*, vol. 67, no. 10, pp. 4042–4054, Oct 2019.
- [33] H. L. V. Trees, *Optimum Array Processing: Part IV of Detection, Estimation, and Modulation Theory*. Wiley, 2002. [Online]. Available: <https://doi.org/10.1002/0471221104>
- [34] J.-W. Tao, L. Liu, and Z.-Y. Lin, "Joint DOA, range, and polarization estimation in the fresnel region," *IEEE Trans. Aerosp. Electron. Syst.*, vol. 47, no. 4, pp. 2657–2672, 2011.
- [35] B. Friedlander, "Localization of signals in the near-field of an antenna array," *IEEE Trans. Signal Process.*, vol. 67, no. 15, pp. 3885–3893, 2019.
- [36] C. Giovannetti, N. Decarli, A. Zanella, and D. Dardari, "Asymptotic behavior of localization and sensing in the near field of extremely large aperture arrays," in *Proc. IEEE Int. Conf. on Commun. Work.*, Jun. 2025, pp. 330–335.
- [37] M. A. Richards, *Fundamentals of radar signal processing*. McGraw-Hill, 2005.
- [38] J. Sherman, "Properties of focused apertures in the fresnel region," *IRE Trans. Antennas Propag.*, vol. 10, no. 4, pp. 399–408, 1962.
- [39] M. Cheney and B. Borden, *Fundamentals of Radar Imaging*. Society for Industrial and Applied Mathematics, 2009. [Online]. Available: <https://epubs.siam.org/doi/abs/10.1137/1.9780898719291>
- [40] A. Mariani, A. Giorgetti, and M. Chiani, "Model order selection based on information theoretic criteria: Design of the penalty," *IEEE Trans. Signal Process.*, vol. 63, no. 11, pp. 2779–2789, Jun. 2015.
- [41] D. C. Rife and R. R. Boorstyn, "Multiple tone parameter estimation from discrete-time observations," *The Bell System Technical Journal*, vol. 55, no. 9, pp. 1389–1410, Nov. 1976.
- [42] T. Bacchielli, L. Pucci, E. Favarelli, D. Dardari, and A. Giorgetti, "Bistatic THz sensing with MIMO-OFDM: A two-stage transmission approach with maximum likelihood estimation," May 2025. [Online]. Available: <http://dx.doi.org/10.36227/techrxiv.174741966.67038524/v1>
- [43] A. S. Rahmathullah, A. F. Garcia-Fernandez, and L. Svensson, "Generalized optimal sub-pattern assignment metric," in *2017 20th International Conference on Information Fusion (Fusion)*, Xi'an, China, Jul. 2017, pp. 1–8.
- [44] E. Matricardi, L. Pucci, E. Favarelli, E. Paolini, and A. Giorgetti, "Multi-target acquisition in multistatic MIMO-OFDM joint sensing and communication," in *Proc. IEEE Int. Conf. Commun. Workshops (ICC Workshops)*, Montreal, QC, Canada, Jun. 2025, pp. 690–695.